

Mitigating Dissolution to Enhance the Performance of Pillar[5]quinone in Sodium Batteries

Md. Adil,^[a] Maximilian Schmidt,^[a] Julia Vogt,^[b, c] Thomas Diemant,^[d] Martin Oschatz,^[b, c, e] and Birgit Esser^{*[a, d]}

Dedicated to Professor Jürgen Janek on the occasion of his 60th birthday

Sodium-ion batteries using organic electrode materials are a promising alternative to state-of-the-art lithium-ion batteries. However, their practical viability is hindered by challenges such as a low specific capacity of the organic electrode materials, or their dissolution in the electrolyte. We herein present a double mitigation strategy to enhance the performance of pillar[5]quinone (P5Q) as positive electrode material in sodium batteries. Using 5 M sodium bis(fluorosulfonyl)imide in succinonitrile as highly concentrated electrolyte, as well as encapsulating P5Q in CMK-3 (Carbon Mesostructured by KAIST with hexagonally ordered rod-like carbon domains) as templated ordered mesoporous carbon, we achieve a record cycling

performance with improved cycling stability even at elevated temperature (40 °C). The P5Q@CMK-3 composite electrode delivers 430 mAh g⁻¹ specific discharge capacity at 0.2 C rate with 90% retention over 200 cycles. This corresponds to an energy density of 831 Wh kg⁻¹ (based on P5Q mass) and surpasses previous reports on pillarquinones. When operated at 40 °C, the P5Q@CMK-3 composite electrodes deliver a specific discharge capacity of 438 mAh g⁻¹ with 88% capacity retention over 500 cycles (0.02% per cycle). This study underscores the crucial role the electrolyte plays in advancing organic sodium batteries, offering a promising avenue for the future of sustainable energy technologies.

1. Introduction

The rise of intermittent energy technologies (solar and wind) demands sustainable energy storage devices based on earth-abundant elements, improved cycle life, and higher energy density with environmental benignity.^[1] This motivates the development of sodium-ion batteries (SIBs) due to their potentially low cost and the large natural abundance of Na (by 2–3 orders of magnitude more than Li).^[2,3] In the quest for more

efficient and sustainable energy storage technologies, organic electrode materials have come into focus as a potentially greener alternative to transition metal oxides (TMOs) and polyanions, such as Na_xM_y(XO₄)_n (X=S, P, Si, As, Mo, and W).^[4] As analogs to TMOs and metal cation-inserting materials, n-type organic compounds such as quinones,^[5] imides,^[6,7] carboxylates,^[8–10] polymeric Schiff bases,^[11] and others^[12] have shown promising performance both in monovalent^[4,9,13] and divalent^[14] metal-ion batteries.^[15] Their structures are adjustable and their electrochemical properties tunable, they can have a high energy density and long cycling stability, and the solid-state diffusion of ions is often not limiting to their performance. Among quinone-based redox-active organic electrode materials, pillarquinones and calixquinones are particularly attractive due to their high theoretical specific capacity (446 mAh g⁻¹) and ease of synthesis.^[5] Each *para*-benzoquinone unit in these macrocycles can be reduced by up to two electrons with concurrent uptake of metal cations from the electrolyte. In addition, these macrocyclic quinones possess a cavity and thus have intrinsic porosity, which can improve ion diffusion in the electrode.^[16] Pillar[5]quinone (P5Q), for instance, features a cavity radius of 4.13 Å with high molecular symmetry.^[17] Both P5Q and calixquinones (calix[n]quinone, n=4, 6, and 8) have been investigated in Li-based half cells,^[18–23] and recently, P5Q and calix[4]quinone (C4Q) were also investigated as positive electrodes in SIBs and other battery chemistries.^[24–28] We herein employ P5Q as positive electrode material, which comprises five *para*-benzoquinone rings connected by methylene units and can provide ten active sites for Na-ion uptake (Figure 1a) after reduction.

[a] M. Adil, M. Schmidt, B. Esser

Institute of Organic Chemistry II and Advanced Materials, Ulm University,
Albert-Einstein-Allee 11, 89081 Ulm, Germany
E-mail: birgit.esser@uni-ulm.de
Homepage: <https://www.esserlab.com>

[b] J. Vogt, M. Oschatz

Institute for Technical Chemistry and Environmental Chemistry, Friedrich Schiller University Jena, Philosophenweg 7a, 07743 Jena, Germany

[c] J. Vogt, M. Oschatz

Center for Energy and Environmental Chemistry Jena (CEEC Jena), Friedrich Schiller University Jena, Philosophenweg 7a, 07743 Jena, Germany

[d] T. Diemant, B. Esser

Helmholtz Institute Ulm (HIU) Electrochemical Energy Storage,
Helmholtzstraße 11, 89081 Ulm, Germany

[e] M. Oschatz

Helmholtz Institute for Polymers in Energy Applications Jena (HIPOLE Jena),
Lessingstraße 12–14, 07743 Jena, Germany

 Supporting information for this article is available on the WWW under
<https://doi.org/10.1002/batt.202400312>

 © 2024 The Authors. *Batteries & Supercaps* published by Wiley-VCH GmbH.
This is an open access article under the terms of the Creative Commons Attribution License, which permits use, distribution and reproduction in any medium, provided the original work is properly cited.

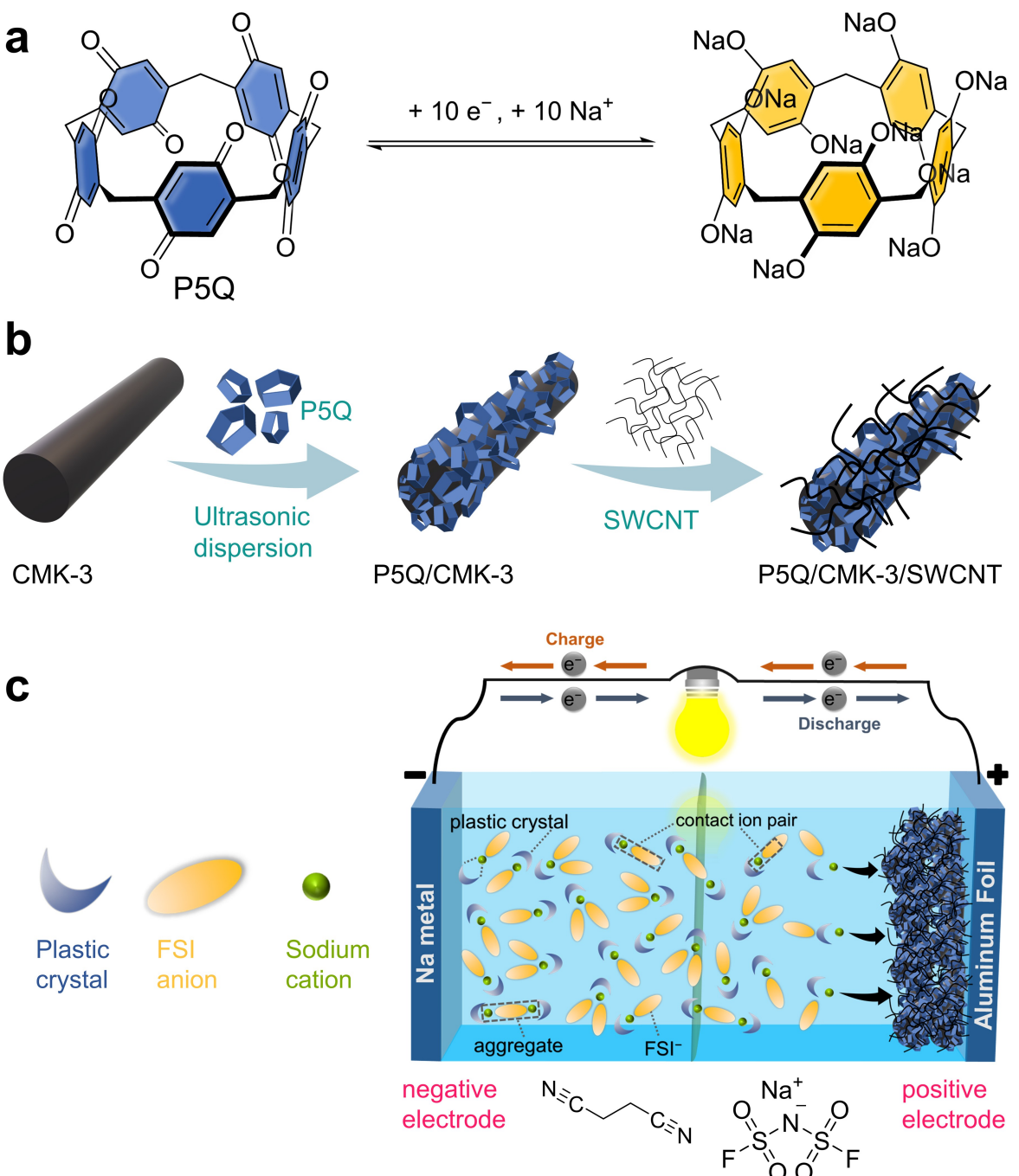


Figure 1. Concept of the P5Q@CMK-3 composite electrode | Na cell. (a) Ten electron-reduction with Na-ion uptake of P5Q; (b) Schematic illustration of the P5Q@CMK-3 composite and electrode preparation. (c) Schematic of the working principle of the battery with the highly concentrated electrolyte.

As these macrocyclic quinones in their neutral or reduced state are usually soluble in aprotic liquid battery electrolytes, which severely reduces their cycling stability, a mitigation strategy has to be applied. These strategies generally include carbon encapsulation, salt formation of the active material, or polymer incorporation.^[6,29–32] While salt formation or polymer incorporation require additional synthetic steps, incorporation into a mesoporous carbon or the use of composite polymer electrolytes enables directly using the small organic molecule

as electrode material.^[18,24] However, these strategies can only mitigate but not completely eliminate the dissolution issue. Therefore, we herein focus on combining two different mitigation strategies to improve the performance of P5Q as electrode material. The first is the inclusion in CMK-3 (Carbon Mesostructured by KAIST with hexagonally ordered rod-like carbon domains) as templated ordered mesoporous carbon. The second is the application of a highly concentrated electrolyte (HCEs) as effective approach to inhibit the dissolution of

active materials into liquid electrolytes. Generally, when the salt concentration is above 3 M, the HCE definition applies, as salt outnumbers the solvent in the binary solution.^[33] A few studies have been reported with quinone-based electrode materials utilizing HCEs in LIBs,^[21,22,34] but most of them suffer from poor cycling stability and lack in-depth mechanistic understanding. HCEs have been reported for SIBs,^[35] but not yet using quinone-based electrodes. Apart from their capability of hindering the dissolution of small organic molecules, HCEs have further advantages as compared to conventional liquid electrolytes due to their peculiar solvation structure.^[36,37]

In a combination of two mitigation strategies to enable superior cycling performance of P5Q in Na-based batteries, we herein employ sodium bis(fluorosulfonyl)imide (NaFSI) dissolved in succinonitrile (SN) at various molar concentrations (1 M, 3 M, and 5 M) as electrolyte in conjunction with the P5Q@CMK-3 composite electrode in Na-based cells. We employ P5Q as composite with the mesoporous carbon CMK-3 to decrease dissolution, and single-walled carbon nanotubes (SWCNTs) for conductivity (Figure 1b) as composite electrode in SIBs with NaFSI in SN electrolytes (Figure 1c). A comparative investigation of different electrolyte concentrations (1 M, 3 M, and 5 M) reveals that the 5 M HCE delivers a much-improved specific capacity and long-term cyclability when compared to state-of-the-art 1 M electrolyte even at elevated temperature (40 °C). Using 5 M NaFSI/SN as electrolyte, the P5Q composite electrode delivers 430 mAh g⁻¹ as second cycle specific discharge capacity ($C_{\text{theo}} = 446 \text{ mAh g}^{-1}$) at 0.2 C rate with ~90% retention over 200 cycles. Furthermore, the Na|5 M|P5Q cell exhibits an excellent energy density of 830 W h kg⁻¹ (based on the mass of P5Q active material in the positive electrode) with a higher average cell potential (~2.01 V) compared to previous reports on P5Q in SIB^[24] and minimal voltage hysteresis even at high current rates (1 C). This serves as a significant leap forward in comparison to previous reports on quinone-based SIBs. Ex-situ Raman spectroscopy reveals the electronic coordination structure of the electrolyte at various salt concentrations, and further ex-situ characterization techniques (FT-IR, XPS) were employed to investigate the reaction mechanism with the HCE. This work opens an avenue to further investigate small molecule quinone-based electrode materials in highly concentrated electrolytes in rechargeable SIBs.

2. Results and Discussion

2.1. Preparation and Characterization of P5Q and the P5Q@CMK-3 Composite

P5Q was synthesized according to a modified procedure by Shurpik et al.^[38] (see Supporting Information, Scheme S1) with optical images of the as-prepared powder in Figure S1. The structure of P5Q was confirmed by ¹H and ¹³C nuclear magnetic resonance (NMR) spectroscopy and high-resolution mass spectrometry (Figure S2). The morphology of P5Q was investigated using field-emission scanning electron microscopy (FE-SEM), revealing a random morphology with different shapes and size

(Figure S3a). The chemical structure was further evaluated using ex-situ Fourier-transform infrared spectroscopy (Figure S3b), which shows distinct C=O stretching vibrations at 1650 cm⁻¹ and 1610 cm⁻¹ along with a band at 1246 cm⁻¹ corresponding to a –CH₂– bending mode.^[39] An XPS survey spectrum (Figure S3c) further demonstrates the purity of the material. The C 1s high-resolution spectrum (Figure S3d) can be fitted with peaks at 284.8 and 287.3 eV, assigned to C=C/C–C and C=O species, respectively.^[22,40] Similarly, the peak at 531.8 eV in the O 1s spectrum (Figure S3e) can be attributed to the carbonyl groups (C=O) of P5Q^[22,40] (see Table S1 for fitting parameters). Gel-permeation chromatography confirms the purity of P5Q (Figure S4a), and thermal gravimetric analysis shows a weight loss with onset at 131 °C, which might be indicative of enclosed solvent molecules, and decomposition onset at 361 °C (Figure S4b). The UV-vis spectrum in CH₂Cl₂-solution (Figure S4c) shows a strong absorption band centered at 249 nm ($\epsilon = 12.8 \times 10^4 \text{ M}^{-1} \text{ cm}^{-1}$) with a small shoulder at around 330 nm, which is in accordance to literature.^[24] Scanning electron microscopy (SEM) with energy-dispersive X-ray spectroscopy (EDS) elemental mapping reveals a uniform distribution of carbon and oxygen in P5Q (Figure S5).

To inhibit the dissolution of P5Q in the liquid battery electrolyte, it was encapsulated within the high surface area mesoporous carbon CMK-3 (specific surface area = 1544 m² g⁻¹, total pore volume = 1.39 cm³ g⁻¹) through a solution-impregnation method employing DMSO as a solvent, which resulted in P5Q@CMK-3 with a weight ratio of 1:2.^[24] Details are provided in the Supporting Information. The nitrogen physisorption isotherm of the CMK-3^[41] (Figure S6a) can be classified as a type IV (a) isotherm with a H1 hysteresis due to capillary condensation indicating the presence of defined mesoporosity. In accordance, the quenched solid density functional theory (QSDFT) pore-size distribution of the carbon (Figure S6b) shows the presence of mesopores with a narrow size-distribution centered at slightly below 5 nm. The SEM images of P5Q, CMK-3, SWCNTs, P5Q@CMK-3 composite powder, and the P5Q@CMK-3 composite cathode (Figure S7) reveal significant differences between pristine P5Q and the P5Q@CMK-3 composite. Pristine P5Q shows a random morphology, whereas CMK-3 has a bundle-like structure (Figure S7a, b). However, after encapsulation, the primary CMK-3 aggregates over the P5Q to form a composite cluster (Figure S7d-f). SWCNTs (Figure S7c) were used as conductive additive, as they can form a three-dimensional conductive framework around the P5Q@CMK-3 composite. SEM/EDS elemental mappings demonstrate a homogenous distribution of carbon and oxygen in the P5Q@CMK-3 composite (Figure S8). Figure S9a shows the X-ray diffraction patterns of the pristine P5Q, CMK-3 as well as the P5Q@CMK-3 composite. The sharp diffraction peak at $2\theta = \sim 7^\circ$ suggests good crystallinity of P5Q. The broad peak in CMK-3 carbon suggests an amorphous state and is consistent with previous reports.^[31] The sharp peak of P5Q at $2\theta = \sim 7^\circ$ is suppressed in the composite (P5Q@CMK-3) indicating an amorphous morphology for the latter after encapsulation of P5Q in CMK-3. The Raman spectra of P5Q show a broad feature at 1373 cm⁻¹ followed by a sharp peak at 1594 cm⁻¹ (Figure S9b), while the

characteristic D and G band of the CMK-3 carbon are located at 1335 cm^{-1} and 1598 cm^{-1} , respectively.^[42] In the P5Q@CMK-3 composite, the sharp peak of P5Q overlaps with the G-band peak of CMK-3. Nevertheless, the characteristic signal for the CMK-3 carbon remains visible, which might suggest effective encapsulation of P5Q within the CMK-3 carbon structure.

The final composite electrode was prepared by mixing SWCNTs (30 wt%) and PVDF binder (10 wt%) with the composite (P5Q@CMK-3, 60 wt%) in NMP as solvent, resulting in a composition of P5Q: CMK-3: SWCNTs: PVDF (20:40:30:10 wt %).^[24] The P5Q mass loading was in the range of 0.8–0.9 mg cm^{-2} . The optical image of the as-prepared electrode is shown in Figure S9c. To elucidate the importance of the composite formation with CMK-3, a conventional electrode with similar mass loading containing only P5Q, SWCNT, and PVDF was also prepared for comparison (details in the Supporting Information).

2.2. Evaluation of the Electrolyte Coordination Structure

The highly concentrated NaFSI in SN electrolyte was studied in detail by Yamada and coworkers.^[33] NaFSI exhibits flexibility in its solvent blending across a broad concentration spectrum due to its minimal cation-anion binding energy.^[43] The SN solvent possesses the capability to dissolve a variety of salts at elevated concentrations, owing to its high dielectric constant and the presence of two nitrile groups as coordination sites for cations.^[44] SN undergoes a transition into a plastic crystal phase at room temperature while retaining its ionic conductivity, facilitated by its molecular re-orientational dynamics.^[45,46] Furthermore, unlike the unstable SEI generated from conventional EC-based electrolytes (i.e. NaPF₆ in ethylene carbonate^[47]), highly concentrated SN-based electrolytes produce an SEI enriched with products derived from anions (Figure S10).^[21,33] This film is regarded as a means to kinetically stabilize the electrode/electrolyte interface.^[35,48] A similar concept has recently been examined with hard carbon electrodes in SIBs.^[33] Despite these merits, only a few reports exist with SN-based HCEs in conjunction with the quinone-based electrode materials. A thorough assessment of SN-based HCE is still lacking for small molecule organic materials to achieve satisfactory cycling performance and a comprehensive mechanistic understanding.^[21,23]

To investigate the effect of the salt concentration on the coordination structure of the NaFSI in SN electrolyte, Raman spectra were recorded at various molar concentrations (Figure S11). In agreement with the results reported by Takada et al.,^[33] a strong effect is seen with increasing salt concentration. The peak at 720 cm^{-1} is ascribed to the stretching vibration of the free FSI anion or the solvent-separated ion pairs, which are not directly attached to the cation, whereas the peak at 731 cm^{-1} is attributed to contact ion pairs (CIPs) (Figure S11a).^[49,50] With increasing salt concentration this peak is shifted to higher wavenumbers owing to a strong bond formation between the ions and the formation of CIPs and

aggregates (AG I and AG II) with wave numbers between 730 and 755 cm^{-1} .^[50]

Furthermore, the coordination state of the SN solvent is significantly affected with an increase in the salt concentration (Figure S11b). The Raman band of the free SN solvent assigned to the C≡N bond is located at 2253 cm^{-1} .^[51] With added NaFSI salt, a shoulder, and later peak appear at an approximate wave number of 2260 cm^{-1} , which increases in intensity with the salt concentration indicating coordination of the C≡N groups by Na⁺ cations. In the highly concentrated 5 M electrolyte, this peak has (according to the peak fitting) a higher intensity than that of the free nitrile groups.

2.3. Investigation of P5Q and the P5Q@CMK-3 Composite for Electrochemical Energy Storage

P5Q possesses five *para*-benzoquinone rings connected by methylene units, which can uptake up to ten electrons (Figure 1a). The calculated low LUMO energy level of -3.93 eV confirms its ability for reduction (Figure S12a, Table S2). The electrochemical performance of P5Q was first evaluated in Li-based half-cells to obtain information on the obtainable specific capacity. A conventional composite electrode was prepared consisting of P5Q, Ketjen Black, and PVDF binder (30:60:10 wt %, for details, see the Supporting Information). 1 M LiPF₆ in EC/DMC (1:1) was used as electrolyte. The cyclic voltammograms (CV) within the 1.8–3.3 V potential range (Figure S12b) show a clear reduction peak and oxidation peak located at 2.62 V and 2.95 V versus Li⁺ | Li, respectively, corresponding to the (de)lithiation of the P5Q electrode, and an overall shape typical for a Faradaic-dominated charge storage process.^[52] The electrode exhibits a high initial specific discharge capacity of 406 mAh g⁻¹ (Figure S12c), corresponding to 91% of its theoretical specific capacity (446 mAh g⁻¹), with a distinct plateau during both charge and discharge (all capacities herein are reported per mass of P5Q as active material). This capacity is indicative of a high utilization of the carbonyl redox-active sites in P5Q, and is comparable or even better than those of previous reports on P5Q.^[18,34] However, the capacity rapidly fades during cycling (Figure S12d), which is likely caused by the dissolution of the active material into the electrolyte. Furthermore, for a comparative study, the similar conventional composite electrode (P5Q, Ketjen Black-600, and PVDF binder (30:60:10 wt%)) was evaluated in Na-based half-cells using 5 M NaFSI in SN electrolyte. The CV (Figure S13a, b) within the 1.3–3.5 V voltage range shows an oxidation and a reduction peak within the range of 2.40–2.66 V and 2.69–2.27 V vs. Na⁺ | Na, respectively. These peaks correspond to the (de)sodiation of the P5Q electrode with a dominant pseudocapacitive charge storage process. The decrease in the peak current with the subsequent cycles indicates the dissolution of the active material. The electrode delivers 320 mAh g⁻¹ (calculation is based on the mass of P5Q as active material) as a second cycle discharge capacity with a well-defined charge-discharge plateau (Figure S13c) corresponding to the peak position in the CV results. Akin to Li-based half-cell, the specific capacity gradually reduces

during cycling (Figure S13d) mainly owing to the dissolution of the active material into the electrolyte.

Hence, we proceeded with investigating the P5Q@CMK-3 composite electrode in SIBs using the NaFSI in SN electrolyte in various concentrations (Figure 2). 5 M was chosen as the highest concentration, as Yamada et al. showed that beyond 5 M the ionic conductivity is largely reduced accompanied by a high viscosity making it unsuitable for battery application.^[33] As shown in Figure S14, the P5Q from the pristine composite electrode does not show significant dissolution in these electrolytes, judged by the lack of coloring after soaking for several hours.

The CVs of the P5Q@CMK-3 electrodes in Na-based half-cell have a shape that indicates a pseudocapacitive charge storage behavior (Figure 2a). This stands in contrast to the CVs in the Li-based half-cell using a conventional P5Q electrode, where clear peaks are visible in the CVs (Figure S12b).^[53] This might be related to the porous structure of the CMK-3 carbon imparting a different storage mechanism on the P5Q@CMK-3 composite

electrode. Furthermore, CMK-3 carbon restrains P5Q's dissolution, thus, the peak shape and potential overlaps with the subsequent cycles, indicating high reversibility and cycling stability in the 5 M NaFSI in SN electrolyte (CVs in the 1 M and 3 M electrolyte are shown in Figure S15c-f). The galvanostatic charge/discharge profiles at 0.2 C rate ($1 \text{ C} = 446 \text{ mAh g}^{-1}$) in the 5 M electrolyte from cycle 2 on show excellent overlap between different cycles with high Coulombic efficiency (Figure 2b). The first cycle (Supporting Information, Figure S16a) shows an activation process of the composite electrode with an initial Coulombic efficiency of 68%, which might be attributed to an interphase formation on the electrode surface.^[34] In accordance to the CVs, the charge/discharge profiles lack plateaus and indicate a pseudocapacitive charge storage mechanism, which is consistent with previous reports.^[24-26] It has been shown that nanosizing can make charge/discharge plateaus disappear,^[54] which might be an effect related to the use of mesoporous CMK-3 herein.

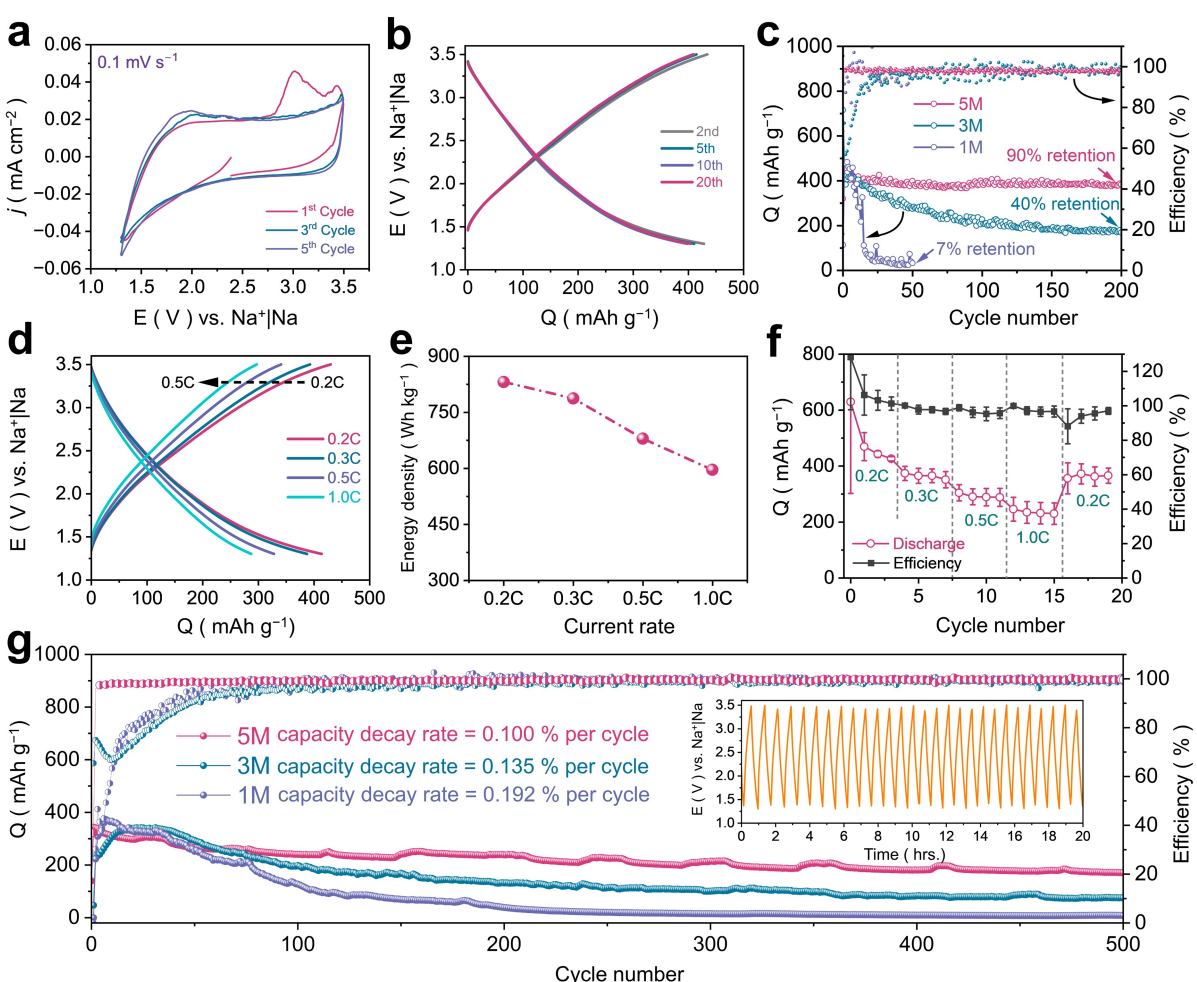


Figure 2. Electrochemical performance of the P5Q@CMK-3 composite electrode (P5Q@CMK-3/SWCNTs/PVDF 60/30/10 wt%) in Na-based cells using NaFSI in SN as electrolyte. (a) CVs at a scan rate of 0.1 mV s^{-1} in 5 M electrolyte. (b) Galvanostatic charge/discharge profiles at 0.2 C in 5 M electrolyte. (c) Comparative cycle-life obtained with the 1, 3, and 5 M electrolyte at 0.2 C (discharge capacities are plotted). (d) Galvanostatic charge/discharge profile at various C-rates in the 5 M electrolyte. (e) Energy density versus current rate plot obtained in the 5 M electrolyte. (f) Specific discharge capacities at various C-rates in 5 M electrolytes, an average of three different cells with error bars. (g) Long-term cycling at 2 C rate with the 1, 3, and 5 M electrolytes (Inset is the voltage versus time plot for the 5 M electrolyte) (specific capacities are given based on the active material P5Q mass).

The P5Q@CMK-3 electrode demonstrates an excellent cycling stability in the 5 M electrolyte at 0.2 C rate (Figure 2c) with a second-cycle specific discharge capacity of 429 mAh g⁻¹ ($C_{\text{spec-theo}} = 446 \text{ mAh g}^{-1}$) (based on active material P5Q mass, 20 wt% of the electrode), of which 90% are retained after 200 cycles, corresponding to only 0.05% capacity fading per cycle. Based on the total mass of the P5Q@CMK-3 composite (60 wt% of the electrode), the specific capacity at 0.2 C rate is 140 mAh g⁻¹ (Figure S17).

Furthermore, the data of constant current cycling at 0.2 C rate for another cell is presented in Figure S18. In contrast, the 1 M and 3 M electrolytes show comparably poor cycling stability (Figure 2c and Figure S16b, c) with a retention of only 40% (168 mAh g⁻¹) and 7% (31.9 mAh g⁻¹) specific discharge capacity over 200 and 50 cycles, respectively. In the 5 M electrolyte, the conductive carbon contributes ca. 80 mAh g⁻¹ to the specific capacity at 0.2 C rate, as shown using an electrode consisting of CMK-3/SWCNT/PVDF in a weight ratio of 80:10:10 (Figure S19). Hence, the presence of P5Q significantly increases the specific capacity of the composite electrode. The superior cycling stability in the 5 M compared to the 1 M or 3 M electrolyte is mainly ascribed to the ability of the HCE to significantly mitigate the dissolution of the active P5Q material. To investigate the effect of mass loading, cycling tests with different mass loadings of P5Q@CMK-3 were performed using the 5 M electrolyte (Figure S20). It is interesting to note that a low loading of the composite exhibited improved capacity and cycling stability in 5 M electrolyte. This may be attributed to the fact that in the low-loading electrode, the electrolyte has more access to the redox-active sites of P5Q due to the shorter diffusion pathway (thin film formation), thus exhibiting higher capacity and stability.

We next investigated the rate capability of the P5Q@CMK-3 composite. At higher C-rates, the charge/discharge profiles in the 5 M electrolyte retain their shape (Figure 2d), while those in the 3 M and 1 M electrolyte show more significant changes (Supporting Information Figure S21). These discharge capacities at the various C-rates in the 5 M electrolyte correspond to high energy densities of 831 Wh kg⁻¹ at 0.2 C and even 596 Wh kg⁻¹ at the high current rate of 1 C (Figure 2e, the energy density calculation is based on the integral method at different current rates from the discharge curves and is based on the P5Q active material mass in the P5Q@CMK-3 composite electrode). The average nominal cell potential, calculated via an integral method (Figure S22a) suggested by Goodenough and co-workers,^[55] is higher in the 5 M compared to the dilute electrolytes, which is consistent with previous reports.^[18,24,25,34,39] At the higher current rate of 1 C, the average nominal cell potential in the 5 M electrolyte is 2.17 V vs. Na|Na⁺, whereas 1.99 V and 2.00 V vs. Na|Na⁺ are obtained in the 3 M and 1 M electrolyte, respectively (Figure S22b). The cycle performance at different C-rates in Figure 2f and Figure S23 shows that in the 5 M electrolyte average reversible discharge capacities of 418, 384, and 334 mAh g⁻¹ are accessible at 0.2 C, 0.3 C, and 0.5 C, respectively. Even at the higher current rate of 1 C, the specific discharge capacity still reaches 289 mAh g⁻¹ (65% of $C_{\text{spec-theo}}$ value) and increases to 389 mAh g⁻¹ when the current is

reduced to 0.2 C. These results further demonstrate the excellent performance of the P5Q@CMK-3 composite electrode with the HCE. In addition, these results outperform previous reports on P5Q and quinone-based positive electrodes in rechargeable organic Li/Na/K-ion batteries (Table S3) using a solid-state electrolyte, dilute/concentrated liquid or ionic-liquid electrolytes.^[18,20,22,24–26,34,39,56]

We next investigated the long-term cycling performance of the P5Q@CMK-3 electrodes in the differently concentrated electrolytes at a 2 C rate (Figure 2g). In the 5 M electrolyte, an excellent long-term cycling stability is obtained with 170 mAh g⁻¹ retained discharge capacity after 500 cycles, corresponding to only 0.1% capacity decay per cycle. In the 3 M and 1 M electrolyte, in comparison, a stronger capacity decay of 0.14% and 0.19% per cycle was observed, resulting in 76 mAh g⁻¹ and 8 mAh g⁻¹ of specific discharge capacity after 500 cycles, respectively. In the 5 M electrolyte, the Coulombic efficiency lies above 99% from the initial cycle on, whereas in the 3 M and 1 M electrolytes, initial activation cycles are necessary to reach a Coulombic efficiency close to 99%. The average discharge potential of the composite electrode in the 5 M electrolyte remains at ca. 2.00 V vs. Na⁺ | Na after 500 cycles (inset of (Figure 2g)), further demonstrating the cycling stability and superiority of the HCE. This average discharge potential is consistent with the previous reports.^[24–26,56] In a long-term cycling experiment at a 1 C rate (1000 cycles), we also obtained a better performance for the 5 M compared to the 3 M and 1 M electrolytes (Figure S24). These results surpass previous reports on P5Q or C4Q in SIBs,^[24–26] and are also remarkable in comparison to other organic positive electrode materials in SIBs (Table S3). The excellent energy storage performance is attributed to the stability of the P5Q@CMK-3 composite electrode in 5 M HCE when compared to dilute 1 M and 3 M electrolytes, as judged by the lack of separator color change after long-term cycling (Figure S25). Moreover, the absence of any side reactions between the succinonitrile solvent and the sodium metal anode is crucial for maintaining optimal electrochemical performance (Figure S26).

The P5Q@CMK-3 | 5 M | Na cell can power a light-emitting diode for around 4 hours with merely one coin-cell (Figure S27). Furthermore, a self-discharge experiment was conducted by holding the fully charged cell (3.5 V) at the open-circuit voltage for ten hours and monitoring the voltage and specific discharge capacity decay (Figure S28). The results show an 88% voltage retention after 10 hours of rest after charging it to the upper cut-off voltage. Such a low voltage decay indicates the absence of any side reactions with the HCEs.

To elucidate the role of CMK-3 for the encapsulation of P5Q in the composite electrode, for comparison a conventional electrode (P5Q/SWCNT/PVDF: 30:60:10 wt%) was investigated in a Na-based half-cell using the 5 M NaFSI in SN electrolyte (for details see the Supporting Information). At a 0.2 C rate, the P5Q@CMK-3 composite electrode delivers a higher fourth cycle discharge capacity of 435 mAh g⁻¹ ($C_{\text{theo}} = 446 \text{ mAh g}^{-1}$) than the conventional electrode of 370 mAh g⁻¹ (Figure S29a). During galvanostatic cycling (Figure S29b), the composite electrode retains 89% of its specific capacity over 120 cycles with only

0.09% capacity decay, while the non-composite electrode shows capacity fading from the initial cycles on with poor capacity retention (43%) and a high rate of capacity decay (0.14% per cycle). This excellent cyclability proves that the CMK-3 carbon encapsulation in conjunction with the HCE further restricts the active material dissolution. Similarly, at increased C-rates (Figure S29c) the P5Q@CMK-3 composite electrode provides higher specific capacities than the conventional electrode. This enhanced performance is attributed to the mesoporous structure of the CMK-3 carbon, which facilitates efficient electron transport, thereby contributing to the superior rate capability of the composite electrode. These results confirm the significant role of CMK-3 carbon encapsulation in improving

the electrochemical performance of the small molecule P5Q electrode.

2.4. Electrochemical Kinetics and Mechanistic Investigations

The electrode kinetics were analyzed to elucidate the electron transport and Na^+ -diffusion into the P5Q@CMK-3 composite electrode using CV at different scan rates (Figure 3a). The broad shape of the CVs indicates that the charge-storage process is mostly surface-dominated and pseudo-capacitive in nature. In order to quantify the contributions from capacitive- vs. diffusion-controlled charge storage, we applied Dunn's method.^[57] The capacitive-like (non-diffusion-limited) current is

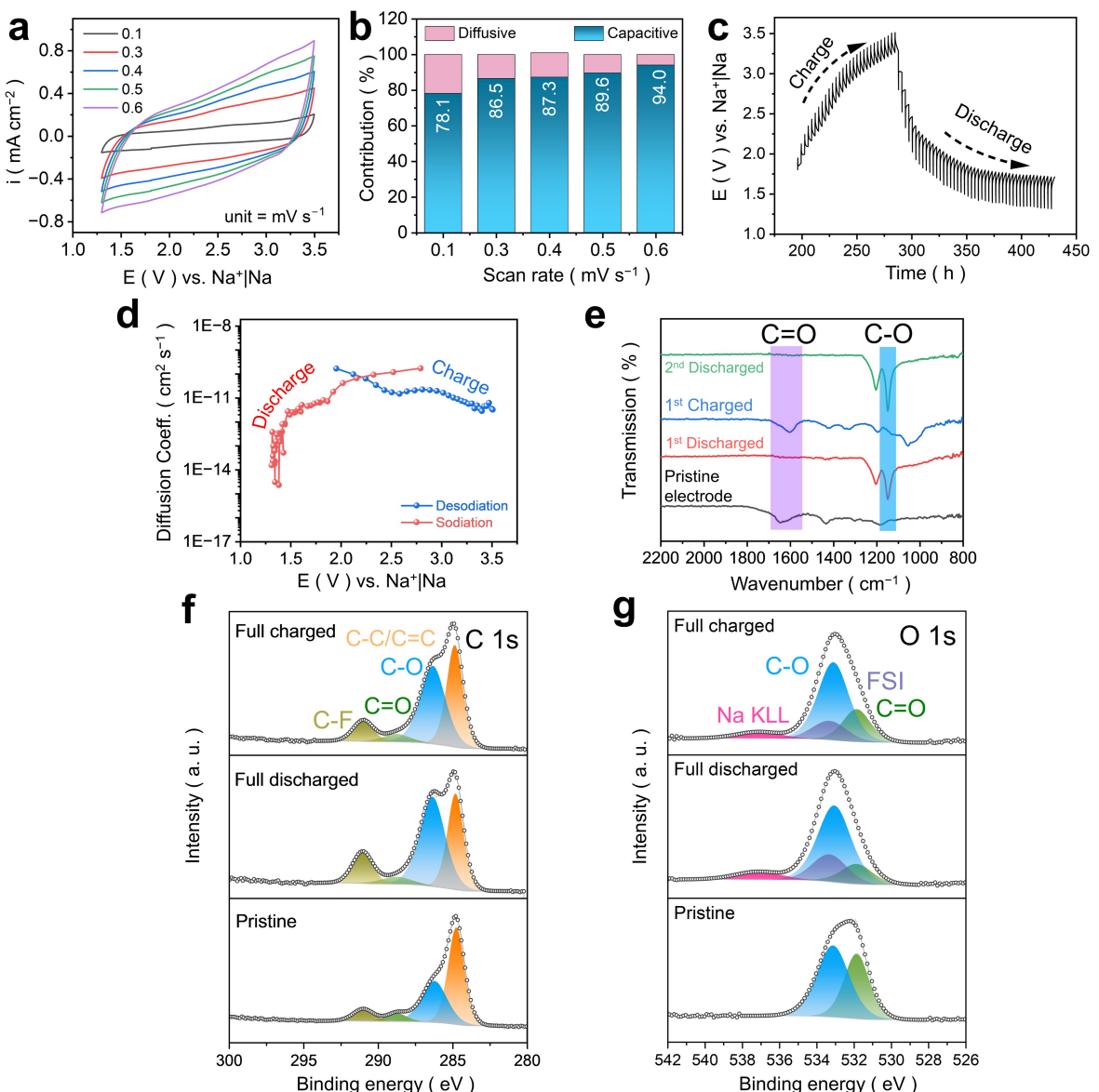


Figure 3. Kinetics and post-cycling analysis of the P5Q@CMK-3 composite electrode from measurements in Na-based half-cells using the 5 M NaFSI in SN electrolyte. (a) CV profiles of the P5Q@CMK-3 composite electrode at different scan rates. (b) Normalized capacitive and diffusion-controlled contribution at different scan rates. (c) Voltage versus time plot from GITT measurements with constant pulses (0.2 C); (d) Na^+ diffusion coefficient (D_{Na^+}) calculated from GITT measurements. (e) Ex-situ FTIR spectra at different states of charge. (f, g) Ex-situ XPS detail spectra in the C 1s and O 1s region at different states of charge.

proportional to the scan rate v , while the diffusion-limited current is proportional to \sqrt{v} . The total current can be expressed as:

$$i(V) = k_1 v + k_2 \sqrt{v} \quad (1)$$

with the parameters k_1 and k_2 . Plotting $\frac{i(V)}{\sqrt{v}}$ versus \sqrt{v} provides a straight line with slope k_1 and intercept k_2 , and thus the fractions of the current stemming from surface-controlled capacitive vs. diffusion-limited processes can be determined.^[58] The current values were calculated at every point on the reduction and oxidation curve of the CVs recorded at different scan rates at intervals of 50 mV. Figure S30 shows a typical fitted CV with 87% capacitive contribution at a scan rate of 0.3 mV s⁻¹. Typically, the surface-controlled capacitive current increases with the scan rate.^[59] Figure 3b shows that this is also the case for the P5Q@CMK-3 composite electrode, where the capacitive-controlled current increases from 78% to 94% with growing scan rate from 0.1 to 0.6 mV s⁻¹. Thus, the fast kinetics of the composite electrode are likely enabled by the porous morphology of the CMK-3 carbon (Figure S7), which effectively reduces the length of the ion diffusion pathways between electrolyte and redox-active center and accelerates the electrochemical redox reactions.

To gain further insight into the Na⁺-ion diffusion kinetics, a galvanostatic intermittent titration technique (GITT) experiment was conducted with a current pulse of 0.2 C for ten minutes followed by a three hours relaxation period to let the cell voltage reach a steady state (for details and equation see the Supporting Information, text and Figure S31).^[60] The corresponding voltage versus time plot is given in Figure 3c. During desodiation (charge) the calculated average diffusion coefficients (D_{Na^+}) are relatively high throughout the whole voltage range (Figure 3d, average value 2.16×10^{-11} cm² sec⁻¹). During sodiation (discharge), the diffusion coefficients are also high until a voltage of ca. 1.47 V is reached, from which point on diffusion becomes much slower. At the end of discharge, the D_{Na^+} value drops, indicating that the diffusion of sodium ions is relatively sluggish owing to the phase transition.^[61] However, the calculated D_{Na^+} value is relatively high throughout the charging process. These results show that the desodiation process is kinetically more favorable than sodiation in the P5Q@CMK-3 composite electrode. The calculated average diffusion coefficient for the composite electrode is 1.29×10^{-11} cm² sec⁻¹, which is in line with or even better than most reported positive electrodes in SIBs ($\sim 10^{-12}$ to 10^{-9} cm² sec⁻¹, Table S4).

The charge storage mechanism of the P5Q@CMK-3 composite with reversible uptake of Na⁺-ions was investigated at different states of charge and discharge state by ex-situ FTIR spectroscopy (Figure 3e) using a 2:1 (P5Q: CMK-3) composite electrode (see SI for details). During sodiation (discharge) the band for the stretching vibration of the carbonyl (C=O) bonds in P5Q at 1645 cm⁻¹ disappears, while a new band at 1150 cm⁻¹ arises due to the reduction of the benzoquinone moieties followed by an aromatization reaction that results in C–O single bonds with coordinated Na⁺ ions (see Figure 1a). During

desodiation (charge), oxidation to the benzoquinones recovers the C=O bonds, concurrent with a disappearance of the C–O stretching vibrations. This result confirms that the carbonyl moieties in P5Q are the redox-active centers and participate in the charge/discharge process. To investigate further structural changes, ex-situ Raman spectroscopy was performed (Figure S32). The characteristic peaks of P5Q at 1594 cm⁻¹ and 1373 cm⁻¹ (Figure S9) overlap with the characteristic bands of the carbon additives (D-bands at 1335 cm⁻¹ and G-band at 1598 cm⁻¹), and hence no significant changes are visible.

To further illustrate the reversible changes in the P5Q@CMK-3 composite electrode during the (de)sodiation process, ex-situ XPS was employed (Figure 3f, g, survey spectra are given in Figure S33 and fitting parameters in Table S5). As indicated in Figure 3f, the C 1s spectra can be fitted with four different peaks, corresponding to the contributions of C–C/C=C, C–O (with PVDF-CH₂), C=O, and C–F species. The carbonyl groups (C=O) primarily originate from P5Q, while the occurrence of C–O bonds in the pristine electrode can most probably be attributed to the carbon additives.^[39] It should be mentioned that the CH₂ groups of the PVDF binder also contribute to the C–O peak; the intensity of this contribution should equal that of the C–F peak (PVDF-CF₂). In the discharged state, the intensity of the C=O peak is lowered while that of the C–O peak increases, which correlates well with the formation of C–O single bonds in the reduced form of P5Q (see Figure 1a). After full charge, on the other hand, the intensity of the C–O peak is reduced again, which indicates re-oxidation to the C=O moieties. In the O 1s spectra, the reversible change in the C–O bond can clearly be seen (Figure 3g). In the discharged state, the intensity of the C=O peak is significantly reduced due to the aromatization and formation of C–O bonds. This is most significant in the first discharge of the pristine electrode, during which the intensity ratio of the C–O (533.0 eV) to the C=O (531.7 eV) peak increases from 1.4:1 to 4:1. After the following charge, the ratio is reduced to 2.6:1, which suggests efficient re-oxidation of P5Q and re-formation of the carbonyl moieties (C=O bonds). It should be mentioned that a peak due to FSI⁻ was inserted into the O 1s spectra of the cycled electrode (533.3 eV, cf. experimental section in the Supporting Information for more details). In addition, the Na Auger feature is observed at 537.1 eV for the cycled electrodes, which is in agreement with the literature.^[40] Furthermore, the appearance of the Na 1s peak in the survey spectrum after the discharge (and the decrease of its intensity in the following charge, cf. Figure S33) confirms the insertion of Na⁺ ions concurrent with the reduction of the P5Q during discharge (as well as the reverse process during charge). The above results are further supported by SEM-EDS studies (Figure S34–S36), which show a lower Na content in the charged compared to the discharged state and overall a uniform distribution of the different components in the electrode surface layer. The SEM images further show that the morphology of the composite electrode remains unchanged after full discharge and charge, even after 1000 cycles at 1 C rate (Figure S37).

To get a detailed insight into the charge transfer resistance and electrochemical kinetics, electrochemical impedance spec-

troscopy (EIS) was performed (Figure S38). Owing to the high viscosity of the HCE, the impedance value in 5 M NaFSI in SN is a little bit higher than in the 3 M and 1 M electrolyte for the initial cycles. However, the impedance of the cells with the 1 M and 3 M electrolytes rapidly increases with cycling (Figure S38a, b), which is likely caused by the dissolution of the active material into the electrolyte.^[22,34] The increase in impedance further suggests the deterioration or the loss of contact between the active material and the conductive carbon during the charge/discharge cycles.^[62] Conversely, the impedance in the HCE (Figure S38c) is comparatively smaller (almost half) than in the dilute electrolyte. The increase in impedance during initial cycling is attributed to the activation process (Figure S38c). After the formation of an ion-conducting solid electrolyte interface (SEI), the charge transfer process becomes more efficient, thus reducing the impedance. The decreasing trend in the impedance (Figure S38c) also demonstrates an improved contact between the active material and the HCE electrolyte during charge-discharge cycling or the occurrence of fast ion transport and electron exchange at the interface. The fast ion transport enables the fast rate capability and rapid diffusion kinetics. Besides, the charge transfer resistance value in HCE is comparatively lower than in dilute electrolytes after 40 cycles (Figure S38d) which is mainly attributed to the formation of an ion-conducting SEI.

2.5. Electrochemical Performance of the P5Q@CMK-3 Composite Electrode at Elevated Temperature in Na-Based Cells

For use of such batteries at elevated temperatures, in, e.g., arid or tropical areas or the well-drilling industry, a reliable operation is essential.^[63,64] However, achieving an optimal battery performance remains a notable challenge at elevated temperatures due to the formation of unstable SEIs and structural deterioration of the active material caused by the rapid transfer of alkali ions.^[63,64] Consequently, there has been an extensive research on Li-ion batteries as high-temperature batteries, attributed to the smaller ion size of Li^+ compared to other alkali ions.^[65] Sodium-ion-based organic batteries are a promising alternative for high-temperature operation due to their thermal stability (most organic materials are stable up to 200 °C). Furthermore, they have high structural flexibility that helps to retain the structural integrity during rapid ion transfer at elevated temperatures,^[66] however, there is still limited evidence in the literature.^[66]

Inspired by the impressive electrochemical performance of the P5Q@CMK-3 composite electrode at room temperature in the HCE, we investigated its electrochemical performance in 5 M, 3 M, and 1 M electrolyte at the elevated temperature of 40 °C in Na-based cells (Figure 4). The charge/discharge profiles (Figure 4a–c) are similar to those obtained at room temperature, however, the reversible specific discharge capacities at 40 °C are higher than those at room temperature owing to the faster Na^+ diffusion. At 40 °C, the second cycle specific discharge capacity is 438 mAh g⁻¹ in the 5 M electrolyte with an impressive 88%

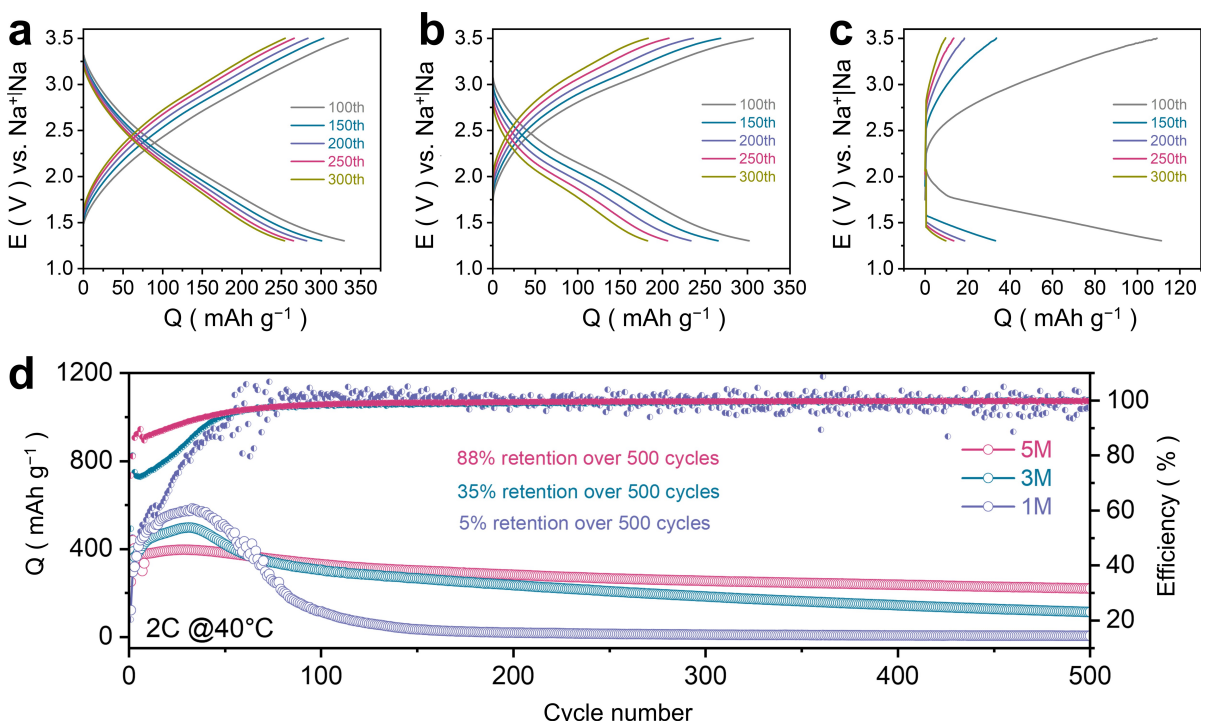


Figure 4. Electrochemical characterization of the P5Q@CMK-3 composite electrode in Na-based cells at elevated temperature (40 °C) using NaFSI in SN. Galvanostatic charge-discharge profiles in (a) 5 M, (b) 3 M, and (c) 1 M electrolyte at 2 C rate with (d) corresponding long-term cycling stability.

retention over 500 cycles (Figure 4d), while at room temperature, the capacity is 344 mAh g^{-1} with a 52% retention over 500 cycles (Figure 2g). The 3 M and 1 M electrolytes deliver specific capacities of 387 and 295 mAh g^{-1} in the second cycle and maintain 35% and 5% capacity at the end of 500 cycles, respectively (Figure 4d). Hence, the HCE exhibits a notably slower capacity decay rate of only 0.02% per cycle when compared to the 3 M (0.13% per cycle) and 1 M (0.19% per cycle) electrolytes, demonstrating an excellent cycling stability of the P5Q@CMK-3 composite electrode in the HCE at elevated temperature. Additionally, the Coulombic efficiency of the composite electrode in the HCE remains consistently close to 100% throughout the long-term cycling. Stabilizing the material surface is an essential key parameter for the electrochemical performance of Li-ion batteries at elevated temperatures as suggested by Amine's group.^[67] Interestingly, the FE-SEM images reveal that the P5Q@CMK-3 composite electrode maintains its structural integrity at the end of 500 cycles, showing a smooth surface with no particle cracking (Figure S39). The performance of the P5Q@CMK-3 composite electrode at elevated temperature not only aligns with but even surpasses that of previous reports on monovalent-ion batteries based on organic materials.^[68,69] Hence, the excellent electrochemical performance at both room- and elevated temperatures suggests that the P5Q@CMK-3 composite electrode, in conjunction with the HCE, stands as a promising candidate for rechargeable organic SIBs.

3. Conclusions

In summary, this study showcases a dual mitigation strategy to obtain a high cycling performance of P5Q in sodium batteries. Using 5 M NaFSI in succinonitrile as a highly concentrated electrolyte (HCE) in conjunction with a CMK-3-carbon-encapsulated P5Q electrode provides excellent cycling performance both at ambient and elevated temperature. The HCE mitigates P5Q dissolution, but still enables rapid and efficient Na^+ diffusion. The P5Q@CMK-3 composite electrode delivers 430 mAh g^{-1} at 0.2 C rate with 90% capacity retention over 200 cycles, outperforming previous reports on pillarquinone-based electrode materials. This corresponds to an impressive energy density of 831 Wh kg^{-1} (based on P5Q active material mass) at 0.2 C, of which 596 Wh kg^{-1} are maintained at a high current rate (1 C). At an elevated temperature of 40°C , the P5Q@CMK-3 delivers a record specific-discharge capacity of 438 mAh g^{-1} with merely 0.02% capacity fade per cycle over 500 cycles. The redox kinetics of the P5Q@CMK-3 electrode has a capacitive-like character, and demonstrates efficient charge transport and Na^+ diffusion. The ex-situ characterization by FT-IR-spectroscopic and XPS measurements confirms the Na^+ storage mechanism with coordination to the carbonyl redox-active centers of P5Q. This work paves the way towards improving the cycling stability of small molecule organic electrode materials in sodium batteries by effective electrode and electrolyte design.

4. Supporting Information

Experimental procedures and additional data can be found in the Supporting Information.

Author Contributions

M.A. and B.E. designed the concept of this project. B.E. directed the research. M.A. performed the P5Q composite synthesis and characterization, all electrode and cell fabrication, electrochemical and kinetics measurements. M.S. synthesized and characterized P5Q and performed the DFT calculations. J.V. synthesized the CMK-3 carbon under the guidance of M.O.. T.D. evaluated the XPS data. M.A. wrote the manuscript with input from B.E.. All authors discussed the results and commented on the manuscript.

Acknowledgements

This work contributes to the research performed at CELEST (Center for Electrochemical Energy Storage Ulm-Karlsruhe). It was funded by the German Research Foundation (DFG) under Project ID 390874152 (POLiS Cluster of Excellence, EXC 2154) and by the European Union (ERC, NanOBatt, 101088146). The authors acknowledge support by the state of Baden-Württemberg through bwHPC and the German Research Foundation (DFG) through grant no INST 40/575-1 FUGG (JUSTUS 2 cluster). Views and opinions expressed are however those of the authors only and do not necessarily reflect those of the European Union or the European Research Council Executive Agency. Neither the European Union nor the granting authority can be held responsible for them. We acknowledge financial support through the state of Baden-Württemberg through bwHPC. Open Access funding enabled and organized by Projekt DEAL.

Conflict of Interests

The authors declare no conflict of interest.

Data Availability Statement

The data that support the findings of this study are openly available at <https://zenodo.org/doi/10.5281/zenodo.10568272>.

Keywords: Small-molecule organic electrodes · concentrated electrolytes · dissolution mitigation · high temperature · sodium-ion batteries

- [1] B. Dunn, H. Kamath, J. M. Tarascon, *Science* **2011**, *334*, 928.
- [2] N. Yabuuchi, K. Kubota, M. Dahbi, S. Komaba, *Chem. Rev.* **2014**, *114*, 11636.
- [3] R. Usiskin, Y. Lu, J. Popovic, M. Law, P. Balaya, Y. S. Hu, J. Maier, *Nat. Rev. Mater.* **2021**, *6*, 1020.

- [4] Y. Lu, C. Jun, *Nat. Chem. Rev.* **2020**, *4*, 127.
- [5] M. Zhang, Y. Zhang, W. Huang, Q. Zhang, *Batteries & Supercaps* **2020**, *3*, 476.
- [6] Z. Song, H. Zhan, Y. Zhou, *Angew. Chem. Int. Ed.* **2010**, *49*, 8444.
- [7] B. Ding, M. Bhosale, T. L. R. Bennett, M. Heeney, F. Plasser, B. Esser, F. Glöcklhofer, *Faraday Discuss.* **2024**, *250*, 129.
- [8] X. Wu, S. Jin, Z. Zhang, L. Jiang, L. Mu, Y. S. Hu, H. Li, X. Chen, M. Armand, L. Chen, X. Huang, *Sci. Adv.* **2015**, *1*, e1500330.
- [9] B. Häupler, A. Wild, U. S. Schubert, *Adv. Energy Mater.* **2015**, *5*, 1402034.
- [10] A. Jouhara, L. Rzesny, V. Rialland, C. Latouche, P. Poizot, B. Esser, *ChemSusChem* **2023**, *16*, e202300286.
- [11] E. Castillo-Martínez, J. Carretero-González, M. Armand, *Angew. Chem. Int. Ed.* **2014**, *53*, 5341.
- [12] M. E. Speer, C. Sterzenbach, B. Esser, *ChemPlusChem* **2017**, *82*, 1274.
- [13] Q. Zhao, Y. Lu, J. Chen, *Adv. Energy Mater.* **2017**, *7*, 1601792.
- [14] Y. Zhang, H. Geng, W. Wei, J. Ma, L. Chen, C. C. Li, *Energy Storage Mater.* **2019**, *20*, 118.
- [15] B. Esser, F. Dolhem, M. Becuwe, P. Poizot, A. Vlad, D. Brandell, *J. Power Sources* **2021**, *482*, 228814.
- [16] P. Seitz, M. Bhosale, L. Rzesny, A. Uhlmann, J. S. Wössner, R. Wessling, B. Esser, *Angew. Chem. Int. Ed.* **2023**, *62*, e202306184.
- [17] A. Allouche, *J. Comput. Chem.* **2011**, *32*, 2716.
- [18] Z. Zhu, M. Hong, D. Guo, J. Shi, Z. Tao, J. Chen, *J. Am. Chem. Soc.* **2014**, *136*, 16461.
- [19] W. Huang, Z. Zhu, L. Wang, S. Wang, H. Li, Z. Tao, J. Shi, L. Guan, J. Chen, *Angew. Chem. Int. Ed.* **2013**, *52*, 9162.
- [20] S. Zheng, H. Sun, B. Yan, J. Hu, W. Huang, *Sci. China Mater.* **2018**, *61*, 1285.
- [21] W. Huang, S. Zheng, X. Zhang, W. Zhou, W. Xiong, J. Chen, *Energy Storage Mater.* **2020**, *26*, 465.
- [22] W. Huang, S. Liu, C. Li, Y. Lin, P. Hu, Z. Sun, Q. Zhang, *EcoMat* **2022**, *4*, 1.
- [23] H. Sun, X. Zhang, M. Zhang, J. Lv, L. Wang, W. Huang, *Org. Electron.* **2020**, *87*, 105966.
- [24] W. Xiong, W. Huang, M. Zhang, P. Hu, H. Cui, Q. Zhang, *Chem. Mater.* **2019**, *31*, 8069.
- [25] S. Zheng, J. Hu, W. Huang, *Inorg. Chem. Front.* **2017**, *4*, 1806.
- [26] B. Yan, L. Wang, W. Huang, S. Zheng, P. Hu, Y. Du, *Inorg. Chem. Front.* **2019**, *6*, 1977.
- [27] X. Wang, Z. Shang, A. Yang, Q. Zhang, F. Cheng, D. Jia, J. Chen, *Chem* **2019**, *5*, 364.
- [28] Q. Zhao, W. Huang, Z. Luo, L. Liu, Y. Lu, Y. Li, L. Li, J. Hu, H. Ma, J. Chen, *Sci. Adv.* **2018**, *4*, eaao1761.
- [29] S. Muench, A. Wild, C. Friebel, B. Häupler, T. Janoschka, U. S. Schubert, *Chem. Rev.* **2016**, *116*, 9438.
- [30] B. Genorio, K. Pirnat, R. Cerc-Korosec, R. Dominko, M. Gaberscek, *Angew. Chem. Int. Ed.* **2010**, *49*, 7222.
- [31] K. Zhang, C. Guo, Q. Zhao, Z. Niu, J. Chen, *Adv. Sci.* **2015**, *2*, 1500018.
- [32] A. Mauger, C. Julien, A. Paolella, M. Armand, K. Zaghib, *Materials (Basel)* **2019**, *12*, 1770.
- [33] K. Takada, Y. Yamada, E. Watanabe, J. Wang, K. Sodeyama, Y. Tateyama, K. Hirata, T. Kawase, A. Yamada, *ACS Appl. Mater. Interfaces* **2017**, *9*, 33802.
- [34] W. Zhang, H. Sun, P. Hu, W. Huang, Q. Zhang, *EcoMat* **2021**, *3*, 1.
- [35] Z. Tian, Y. Zou, G. Liu, Y. Wang, J. Yin, J. Ming, H. N. Alshareef, *Adv. Sci.* **2022**, *9*, 2201207.
- [36] Y. Yamada, A. Yamada, *J. Electrochem. Soc.* **2015**, *162*, A2406.
- [37] Y. Yamada, J. Wang, S. Ko, E. Watanabe, A. Yamada, *Nat. Energy* **2019**, *4*, 269.
- [38] D. N. Shurpik, P. L. Padnya, L. I. Makhmutova, L. S. Yakimova, I. I. Stoikov, *New J. Chem.* **2015**, *39*, 9215.
- [39] W. Zhang, H. Tian, J. Wang, H. Sun, J. Wang, W. Huang, *ACS Appl. Mater. Interfaces* **2022**, *14*, 38887.
- [40] Y. Hu, Q. Yu, W. Tang, M. Cheng, X. Wang, S. Liu, J. Gao, M. Wang, M. Xiong, J. Hu, C. Liu, T. Zou, C. Fan, *Energy Storage Mater.* **2021**, *41*, 738.
- [41] S. Jun, S. Hoon Joo, R. Ryoo, M. Kruk, M. Jaroniec, Z. Liu, T. Ohsuna, O. Terasaki, *J. Am. Chem. Soc.* **2000**, *122*, 10712.
- [42] Z. Li, L. Deng, I. A. Kinloch, R. J. Young, *Prog. Mater. Sci.* **2023**, *135*, 101089.
- [43] E. Jónsson, P. Johansson, *Phys. Chem. Chem. Phys.* **2012**, *14*, 10774.
- [44] Y. Shen, G. H. Deng, C. Ge, Y. Tian, G. Wu, X. Yang, J. Zheng, K. Yuan, *Phys. Chem. Chem. Phys.* **2016**, *18*, 14867.
- [45] P. J. Alarco, Y. Abu-Lebdeh, A. Abouimrane, M. Armand, *Nat. Mater.* **2004**, *3*, 476.
- [46] P. Derollez, J. Lefebvre, M. Descamps, W. Press, H. Fontaine, *J. Phys. Condens. Matter* **1990**, *2*, 6893.
- [47] S. Komaba, W. Murata, T. Ishikawa, N. Yabuuchi, T. Ozeki, T. Nakayama, A. Ogata, K. Gotoh, K. Fujiwara, *Adv. Funct. Mater.* **2011**, *21*, 3859.
- [48] K. Sodeyama, Y. Yamada, K. Aikawa, A. Yamada, Y. Tateyama, *J. Phys. Chem. C* **2014**, *118*, 14091.
- [49] A. Boschin, P. Johansson, *Electrochim. Acta* **2015**, *175*, 124.
- [50] S.-D. Han, O. Borodin, D. M. Seo, Z.-B. Zhou, W. A. Henderson, *J. Electrochem. Soc.* **2014**, *161*, A2042.
- [51] Y. Dai, K. Wang, B. Zhou, M. Du, R. Liu, B. Liu, B. Zou, *J. Phys. Chem. C* **2016**, *120*, 5340.
- [52] Y. Gogotsi, R. M. Penner, *ACS Nano* **2018**, *12*, 2081.
- [53] Y. Jiang, J. Liu, *Energy Environ. Mater.* **2019**, *2*, 30.
- [54] M. Okubo, E. Hosono, J. Kim, M. Enomoto, N. Kojima, T. Kudo, H. Zhou, I. Honma, *J. Am. Chem. Soc.* **2007**, *129*, 7444.
- [55] L. Xue, S. Xin, J. B. Goodenough, C. Austen Angell, *ACS Energy Lett.* **2017**, *2*, 1534.
- [56] H. Li, W. Duan, Q. Zhao, F. Cheng, J. Liang, J. Chen, *Inorg. Chem. Front.* **2014**, *1*, 193.
- [57] T. Brezesinski, J. Wang, S. H. Tolbert, B. Dunn, *Nat. Mater.* **2010**, *9*, 146.
- [58] M. Adil, A. Sarkar, S. Sau, D. Muthuraj, S. Mitra, *J. Power Sources* **2022**, *541*, 231669.
- [59] M. Adil, S. Sau, P. Dammala, S. Mitra, *Energy Fuels* **2022**, *36*, 7816.
- [60] S. D. Kang, W. C. Chueh, *J. Electrochem. Soc.* **2021**, *168*, 120504.
- [61] Z. Xing, Z. Jian, W. Luo, Y. Qi, C. Bommier, E. S. Chong, Z. Li, L. Hu, X. Ji, *Energy Storage Mater.* **2016**, *2*, 63.
- [62] T. Cai, Y. Han, Q. Lan, F. Wang, J. Chu, H. Zhan, Z. Song, *Energy Storage Mater.* **2020**, *31*, 318.
- [63] J. H. Lee, A. S. Lee, J. C. Lee, S. M. Hong, S. S. Hwang, C. M. Koo, *J. Mater. Chem. A* **2015**, *3*, 2226.
- [64] H. Park, S. Choi, S. J. Lee, Y. G. Cho, G. Hwang, H. K. Song, N. S. Choi, S. Park, *Nano Energy* **2016**, *26*, 192.
- [65] S. Ma, M. Jiang, P. Tao, C. Song, J. Wu, J. Wang, T. Deng, W. Shang, *Prog. Nat. Sci.* **2018**, *28*, 653.
- [66] P. Poizot, J. Gaubicher, S. Renault, L. Dubois, Y. Liang, Y. Yao, *Chem. Rev.* **2020**, *120*, 6490.
- [67] Y. K. Sun, Z. Chen, H. J. Noh, D. J. Lee, H. G. Jung, Y. Ren, S. Wang, C. S. Yoon, S. T. Myung, K. Amine, *Nat. Mater.* **2012**, *11*, 942.
- [68] Y. Liang, C. Luo, F. Wang, S. Hou, S. C. Liou, T. Qing, Q. Li, J. Zheng, C. Cui, C. Wang, *Adv. Energy Mater.* **2019**, *9*, 1802986.
- [69] K. Qin, K. Holguin, J. Huang, M. Mohammadiroudbari, F. Chen, Z. Yang, G. L. Xu, C. Luo, *Adv. Sci.* **2022**, *9*, 2106116.

Manuscript received: May 8, 2024

Revised manuscript received: June 27, 2024

Accepted manuscript online: July 2, 2024

Version of record online: September 2, 2024